Biomaterials 32 (2011) 693–705

Contents lists available at ScienceDirect

Biomaterials

journal homepage: www.elsevier.com/locate/biomaterials

Biological actions of silver nanoparticles embedded in titanium controlled by micro-galvanic effects

Huiliang Cao [a], Xuanyong Liu [a,b,*], Fanhao Meng [a], Paul K. Chu [b]

[a] State Key Laboratory of High Performance Ceramics and Superfine Microstructure, Shanghai Institute of Ceramics, Chinese Academy of Sciences, Shanghai 200050, China
[b] Department of Physics and Materials Science, City University of Hong Kong, Tat Chee Avenue, Kowloon, Hong Kong, China

ARTICLE INFO

Article history:
Received 1 September 2010
Accepted 19 September 2010
Available online 20 October 2010

Keywords:
Silver nanoparticles
Titanium
Antibacterial effects
Cytotoxicity
Micro-galvanic effect

ABSTRACT

Titanium embedded with silver nanoparticles (Ag NPs) using a single step silver plasma immersion ion implantation (Ag-PIII) demonstrate micro-galvanic effects that give rise to both controlled antibacterial activity and excellent compatibility with osteoblasts. Scanning electron microscopy (SEM) shows that nanoparticles with average sizes of about 5 nm and 8 nm are formed homogeneously on the titanium surface after undergoing Ag-PIII for 0.5 h and 1 h, respectively. Transmission electron microscopy (TEM) and X-ray photoelectron spectroscopy (XPS) indicate that those nanoparticles are metallic silver produced on and underneath the titanium surface via a local nucleation process from the solid solution of α-Ti(Ag). The Ag-PIII samples inhibit the growth of both *Staphylococcus aureus* and *Escherichia coli* while enhancing proliferation of the osteoblast-like cell line MG63. Electrochemical polarization and Zeta potential measurements demonstrate that the low surface toxicity and good cytocompatibility are related to the micro-galvanic effect between the Ag NPs and titanium matrix. Our results show that the physico-chemical properties of the Ag NPs are important in the control of the cytotoxicity and this study opens a new window for the design of nanostructured surfaces on which the biological actions of the Ag NPs can be accurately tailored.

1. Introduction

Titanium-based implantable devices such as joint prostheses, fracture fixation devices and dental implants, are important to human lives and improvement of the life quality of patients [1]. A serious issue related to these devices is the bacterial infection which is one of the biggest complications following surgery. After adhering onto the device surface, bacteria tend to aggregate in a hydrated polymeric matrix to form a biofilm which is the cause of many types of persistent and chronic bacterial infection [2]. Colonization which may occur at the time of surgery or from bacteria from remote sources where bacteria are seeded at the vicinities of the implants can lead to acute hematogenous infection [3,4]. Therefore, an important strategy is to prevent initial adhesion of bacteria by making the implant antibacterial by for example, coating with an antibacterial film.

Silver (Ag) as a non-specific biocidal agent is able to act strongly against a broad spectrum of bacterial and fungal species including antibiotic resistant strains [5]. It is believed that silver nanoparticles (Ag NPs) are more reactive than the bulk metallic counterpart because of the larger active surface area [6] and various Ag NPs – modified films have been fabricated based on the release-killing path of Ag NPs [7–9]. Some results have shown that the bactericidal properties of Ag NPs are size or shape dependent. Morones et al. [10] reported that only silver particles with a preferentially diameter of about 1–10 nm had direct interactions with bacteria. Elechiguerra et al. [11] reported that the size of silver particles bound to the human immunodeficiency virus (HIV) cells was exclusively in the range of 1–10 nm, and the truncated triangular silver nanoparticles with {111} as the basal plane displayed the strongest bactericidal activity when comparing spherical and rod-shaped nanoparticles with silver ions (in the form of $AgNO_3$) [12]. Hence, Ag NPs may be a promising alternative as a new antibacterial agent due to their ultra-small size and unique chemical and physical properties. However, the ultra-small size and unique properties such as high mobility of Ag NPs also raise concerns about their potential cytotoxicity, how exactly and to what extent do Ag NPs induce cytotoxicity is still not well understood. It has been suggested that diffusing Ag NPs may act as Trojan horses by entering the cells and then releasing silver ions that damage intracellular functions [13]. Kim et al. [14] have, however, argued that the

* Corresponding author. State Key Laboratory of High Performance Ceramics and Superfine Microstructure, Shanghai Institute of Ceramics, Chinese Academy of Sciences, Shanghai, China. Tel./fax: +86 21 5241 2409.
E-mail addresses: xyliu@mail.sic.ac.cn (X. Liu), paul.chu@cityu.eud.hk (P.K. Chu).

0142-9612/$ – see front matter © 2010 Elsevier Ltd. All rights reserved.
doi:10.1016/j.biomaterials.2010.09.066

cytotoxicity of Ag NPs is primarily the result of the oxidative stress and independent of the toxicity of silver ions. The differences may result from the specific changes in the physico-chemical properties of the Ag NPs under different circumstances. For instance, mobile Ag NPs can easily aggregation in the medium and many researchers have used various detergents (or stabilizers) to disperse them but these chemicals may alter the cytotoxic behavior of the Ag NPs. Sur et al. [15] have studied the cytotoxicity and cellular uptake of mobile Ag NPs modified with glucose, lactose, and oligonucleotides in living non-cancer and cancer cells and found that the chemical nature of these ligands strongly influenced the toxicity and cellular uptake in the cells. Other chemical substances used in fabricating Ag NPs, for example, $NaBH_4$ [9,16], may also affect the toxicity [17]. Although their effects have been neglected in a number of studies [18], a better understanding is crucial to the accurate assessment of the cytotoxicity of these particles. Such effort has partially been plagued by the intrinsically easy aggregation of Ag NPs and limited number of techniques to fabricate Ag NPs.

Plasma immersion ion implantation (PIII) is a non-line-of-light process that has been extensively applied to the surface modification of various biomaterials [19,20]. In order to improve the antibacterial properties of biomedical devices and materials [21], silver plasma immersion ion implantation (Ag-PIII) has been developed. The technique has mainly been applied to polymeric materials [22,23]. In this work, Ag-PIII is conducted on commercial pure titanium (Cp Ti) in order to control and probe the biological actions of Ag NPs to bacteria (*Staphylococcus aureus* and *Escherichia coli*) and mammalian cells (osteoblast-like cell line MG63).

2. Materials and experimental details

2.1. Specimen fabrication and characterization

2.1.1. Ag plasma immersion ion implantation (Ag-PIII)

The samples were one-side polished 10 mm square Cp Ti (Grade 2) plates with a thickness of 1 mm (for Ag-PIII) or rectangular plates (20 mm long, 10 mm wide, and 1 mm thick for the zeta potential measurements). Silver was implanted into the polished side using a filtered cathodic arc plasma source. A magnetic duct with a curved shape was inserted between the plasma source and main chamber to remove macro-particles produced from the cathodic arc. The cathode rod 10 mm in diameter was made of 99.99% pure metallic silver. The Ag discharge was controlled by the main arc current between the cathode and anode. By applying a pulsed high voltage to the Cp Ti samples, Ag ions were implanted and the implantation instrumental parameters are listed in Table 1. During Ag-PIII, the main arc current and pulsed high voltage applied to target was synchronized at a pulsing frequency of 6 Hz. The pulse duration of the high voltage was 450 μs which was also the same as that of the main arc current. Prior to plasma implantation, the Cp Ti samples were cleaned for 2 min with a radio frequency (RF) argon (Ar) plasma source at a bias of −500 V. During Ag-PIII, the sample stage was actively cooled by circulating water to keep the sample temperature at 25 °C.

2.1.2. Surface chemistry and structure characterization

The surface morphology of the samples after Ag-PIII was examined by scanning electron microscopy (SEM, JEOL JSM-6700F, Japan) and X-ray diffraction (XRD) spectra were acquired on a PHILIPS X′ Pert MPO Pro X-Ray diffractometer with Cu K_α radiation at 40 kV and 40 mA under the conventional Bragg diffraction (CBD) modes. The elemental depth profiles and Ag chemical states were determined by X-ray photoelectron spectroscopy (XPS) (Physical electronics PHI 5802). The cross-sections of the Ag-PIII samples were investigated by transmission electron microscopy (TEM, JEM2100F). The TEM specimens were thinned using a Gatan 691 ion-thinning system.

Table 1
Important instrumental parameters used in silver plasma ion immersion implantation (PIII).

	Target	Cathodic arc
Voltage pulse duration (μs)	450	450
Pulsing frequency (Hz)	6	6
Ion implantation voltage (kV)	−30	
Ion implantation time (h)	0.5, 1.0, 1.5	
Pressure (Pa)	2.5×10^{-3}	

2.1.3. Silver release

The Ag-PIII titanium samples were incubated for various periods of time in 10 ml water at 37 °C without stirring. The amounts of released silver were determined by analyzing the resulting solutions by inductively-coupled plasma optical emission spectrometry (ICP-OES).

2.1.4. Dynamic potential polarization test

Dynamic potential polarization curves were acquired from the Cp Ti and Ag-PIII samples in a physiological saline solution (0.9% NaCl at a pH of 7) using a CHI760C electrochemical workstation (Shanghai, China). The measurement was conducted using a conventional three-electrode electrochemical cell with a saturated calomel electrode (SCE) as the reference electrode, a graphite rod as the counter electrode, and the sample with a 0.3 cm^2 exposed area as the working electrode. Prior to the polarization test, the samples were stabilized in the solution for 15 min and the tests were conducted at room temperature at a scanning rate 20 mV/min.

2.1.5. Surface zeta potential measurements

The zeta potentials were measured from the Cp Ti and Ag-PIII samples (20 mm long, 10 mm wide, and 1 mm thick) on a Surpass electrokinetic analyzer (Anton Parr, Austria). Determination of the zeta potential was based on the measurement of the streaming potential and current. In the streaming potential measurements, a 0.9% sodium chloride (NaCl) solution with various pH values (regulated by addition of 1M HCl or 1M NaOH solutions) was forced (pumped) to flow along the surfaces of the samples and the potentials resulting from the motion of ions in the diffusion layer were measured according to the following relationship:

$$\zeta = \frac{dU}{dP} \times \frac{\eta}{\epsilon \times \epsilon_0} \times K \quad (1)$$

where ζ is the zeta potential, dU/dp represents the slope of the streaming potential versus pressure, and η, ϵ_0, ϵ and K denote the electrolyte viscosity, vacuum permittivity, dielectric constant of the electrolyte, and conductivity, respectively. The streaming potential or alternatively the streaming current was detected by the electrodes placed at both sides of the sample. The electrolyte conductivity, temperature, and pH value were determined simultaneously.

2.2. In vitro cytotoxicity and cytocompatibility evaluation

2.2.1. Cell culture

The osteoblast-like cell line MG63 (Cells Resource Center, Shanghai Institutes of Biological Science, Shanghai, P.R. China) was seeded on the Cp Ti and Ag-PIII specimens plates to evaluate the cytocompatibility. The cells were firstly cultured at 37 °C in a humidified atmosphere of 5% CO_2 in 75 cm^2 flasks (Corning Incorporated, USA) containing 10 ml of α-minimum essential medium (α-MEM) (Minimum Essential Medium alpha-Medium, Gibco, Invitrogen, Inc), 10% fetal calf serum (FCS) (Excell Biology, Inc, South America), 2 mM L-glutamine (Hyclone, USA), 1% antimicrobial of penicillin, and streptomycin (Antibiotic-Antimycotic, Gibco, Invitrogen Corporation). The culture medium was changed every three days. With regard to the subculture, the cell monolayer was washed twice with a phosphate-buffered saline (pH = 7.4, Gibco, Invitrogen) and incubated in a trypsin-ethylenediaminetetraacetic acid (EDTA) solution (0.25% trypsin, 1 mM EDTA (Chemicon International)) for 5–10 min at 37 °C to detach the cells. The cells were centrifuged at 900 r/min and 28 °C for 6 min and re-suspended in the complete medium for reseeding onto on the Cp Ti and Ag-PIII samples. The specimens with dimensions of $10 \times 10 \times 1$ mm^3 were sterilized in an autoclave at 121 °C for 40 min and put into a 24-well culture plate (Costar, USA). Afterwards, l.0 ml of the cell suspension with a cell density of 1×10^5 cell/ml was added to each well and the culture plate was transferred gently to a 37 °C incubator.

2.2.2. Cell proliferation and viability

The cell proliferation and viability were determined using the alamarBlue™ assay (AbD Serotec Ltd, UK) that measured the accumulative metabolic activity. Five specimens were tested for each incubation period (1, 3, 7, and 9 days). After each incubation period, the culture medium was removed and 1.0 ml of the fresh medium with 5% alamarBlue™ was added to each well. After incubation for 5 h, 100 μl of the culture medium was transferred to a 96-well plate for measurement. Accumulation of reduced alamarBlue™ in the culture medium was determined by an enzyme labeling instrument (BIO-TEK, ELX 800) at extinction wavelengths of 570 nm and 600 nm. The operation procedures and calculation of cell proliferation or viability of cells followed the instruction of the alamarBlue™ assay.

2.2.3. Morphology

After each time point, the specimens were taken out and rinsed with a phosphate-buffered saline solution (pH = 7.2, PBS) twice to remove the unattached cells and fixed with 3% glutaraldehyde solution in a sodium cacodylate buffer (pH = 7.4, Gibco, Invitrogen) for 30 min after removal from the culture plate. Prior to SEM, the specimens were dehydrated in a series of ethanol solutions (30, 50, 75, 90, 95, and 100 v/v%) for 10 min each sequentially, with the final dehydration conducted in absolute ethanol (twice) followed by drying in the hexamethyldisilizane (HMDS) ethanol solution series. In the laser scanning confocal microscopy (LSCM) observation, a l.0 ml cell

suspension with a cell density of 1×10^4 cell/ml was seeded onto the specimen plates. After incubating for 1, 3, 5, and 24 h, the seeded cells were rinsed with PBS (phosphate-buffered saline) three times and fixed in a 3% glutaric dialdehyde diluent for 20 min at room temperature, followed by three rinses with PBS. The cells were permeabilized with 0.2% (v/v) Triton X-100 (Amresco, USA) for 4 min at room temperature followed by three rinses with PBS. They were then stained with mouse anti-vinculin monoclonal antibody (Sigma–Aldrich) at room temperature for 60 min and rhodamine phalloidin (invitrogen detection technologies, USA) at room temperature for 40 min, followed by three rinses with PBS and further staining with DAPI (Chemical International) for 10 min. The cytoskeletal actin, vinculin expression, and cell nuclei were examined by scanning laser confocal microscopy (LSCM, Zeiss Lsm510 meta).

2.3. Antibacterial test

The antibacterial activity on the Cp Ti and Ag-PIII samples was evaluated by the bacterial counting method using *S. aureus* (*S. aureus*, ATCC 25923) and *E. coli* (*E. coli*, ATCC 25922). The specimens were sterilized in an autoclave at 121 °C for 40 min. A solution containing the bacteria at a concentration of 10^8 cfu/ml was introduced onto the sample to a density of 0.06 ml/cm^2. The samples with the bacterial solution were incubated at 37 °C for 24 h. The dissociated bacterial solution was collected and inoculated into a standard agar culture medium. After incubation at 37 °C for 24 h, the active bacteria were counted in accordance with the National Standard of China GB/T 4789.2 protocol. In the SEM examination, a solution containing the bacteria at a concentration of 10^8 cfu/ml was put on the sample to a density of 0.06 ml/cm^2, incubated at 37 °C for 24 h, fixed, and dehydrated according to the same procedures (specified in Section 2.2.3) used on the osteoblast-like cells.

3. Results

3.1. Characterization of the Ag-PIII samples

Fig. 1 shows the microstructure evolution in the titanium samples after undergoing Ag-PIII at 30 kV for 0.5 h, 1.0 h and 1.5 h (designated as 0.5h-Ag-PIII, 1.0h-Ag-PIII, and 1.5h-Ag-PIII, respectively). The original surfaces were flat (Fig. 1a) with polycrystalline α-Ti being the major phase (Fig. 1e). The nanoparticles are homogeneously distributed on 0.5h-Ag-PIII. As shown by the typical SEM image in Fig. 1b, most of the particles are about 5 nm big and there are about 2.8×10^8 particles per square millimeter. As the PIII time increases, the silver concentration increases and the particles become larger (Fig. 1c and d). The peak of the particle size distribution calculated from 1.0h-Ag-PIII is about 8 nm (Fig. 1c) and the particle size distribution range is also broadened. However, as the PIII time increases to 1.5 h, the peak broadening effect is stopped at about 25 nm and the particle density decreases to 1.7×10^8. The particle growth ceases at about 25 nm because the implantation process is carried out at room temperature, and the diffusion kinetics for the silver atoms in the α-Ti lattice is predominately limited by thermodynamics.

The Ag-PIII samples are examined by transmission electron microscopy (TEM). Fig. 2b is a typical bright-field (BF) image of the encircled area in Fig. 2a showing a cross-sectional view of the surface in 1.5h-Ag-PIII. The indexed insert is a selected-area diffraction (SAD) pattern taken from the encircled area revealing that many small face centered cubic (FCC) crystals are embedded in a larger hexagonal close-packed (HCP) crystal. These small face centered cubic (FCC) crystals have different orientations. Furthermore, a typical {111} spacing of 0.238 nm, as shown in Fig. 2c, can be well resolved by high-resolution transmission electron microscopy (HR-TEM). The EDS spectrum acquired from the area (Fig. 2c) further confirms that the small face centered cubic (FCC) crystals are metallic silver crystals, and the HCP diffraction pattern corresponds to the α-Ti phase. As the Ag NPs are embedded in the titanium in single Ag-PIII step, there is no distinct boundary between the silver containing layer and titanium substrate, as shown in Fig. 2b. Hence, the possibility of adhesive failure is lower compared to other coating processes such as plasma spraying [24]. According to the bright-field (BF) image in Fig. 2d, the particle density in 1.0h-Ag-PIII is quite low and the morphology of the particles is also different from that in 1.5h-Ag-PIII. The particles in 1.0h-PIII have equiaxial grains (Fig. 2d) whereas those in 1.5h-PIII have a distorted inequiaxial morphology (Fig. 2b). The results indicate that the particles are initially precipitated via a local supersaturation nucleation process from the solid solution of α-Ti(Ag) and subsequently separated into even smaller segments (Fig. 2c) until approaching the retained dose limitation when the sputtering effect becomes significant. This is the reason why a smaller surface particle density results as the implantation time is lengthened from 0.5 to 1.5 h (Fig. 1b, 1c, and 1d).

The Ag-PIII samples are further investigated by X-ray photoelectron spectroscopy (XPS). Fig. 3 shows the XPS Ag 3d spectra obtained from the surface and at a depth of 10 nm of the 0.5h, 1.0h, and 1.5h-Ag-PIII specimens. The Ag 3d doublet at 374.3 eV (Ag 3d3/2) and 368.3 eV (Ag 3d5/2) corresponds to metallic silver [25]. As shown in Fig. 3a, the doublet located at 375.0 and 369.0 eV which originates from the silver alloyed titanium phases [25] shifts to lower binding energy positions approaching those of metallic silver as the implantation time is increased to 1.5 h (Fig. 3c). There is no evidence of Ag oxidation corroborating that oxide-free Ag NPs are embedded in the titanium. A similar binding energy shift is observed at a depth of 10 nm. The doublet of 0.5h-Ag-PIII is at 374.83 and 368.87 eV (Fig. 3d), whereas that of 1.5h-Ag-PIII shifts to 374.69 eV and 368.71 eV, respectively (Fig. 3f).

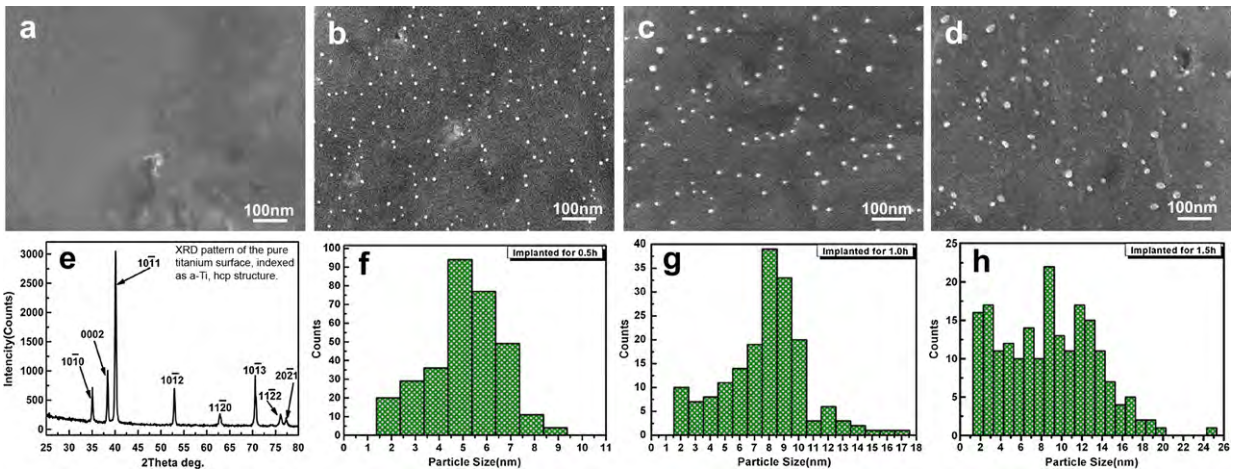

Fig. 1. Surface morphology of the titanium surfaces after Ag-PIII examined by SEM: (a) Cp Ti, (b) 0.5h-Ag-PIII, (c) 1.0h-Ag-PIII, and (d) 1.5h-Ag-PIII, (e) XRD spectra acquired from Cp Ti, and size distributions of the particles on (f) 0.5h-Ag-PIII, (g) 1.0h-Ag-PIII, and (h) 1.5h-Ag-PIII.

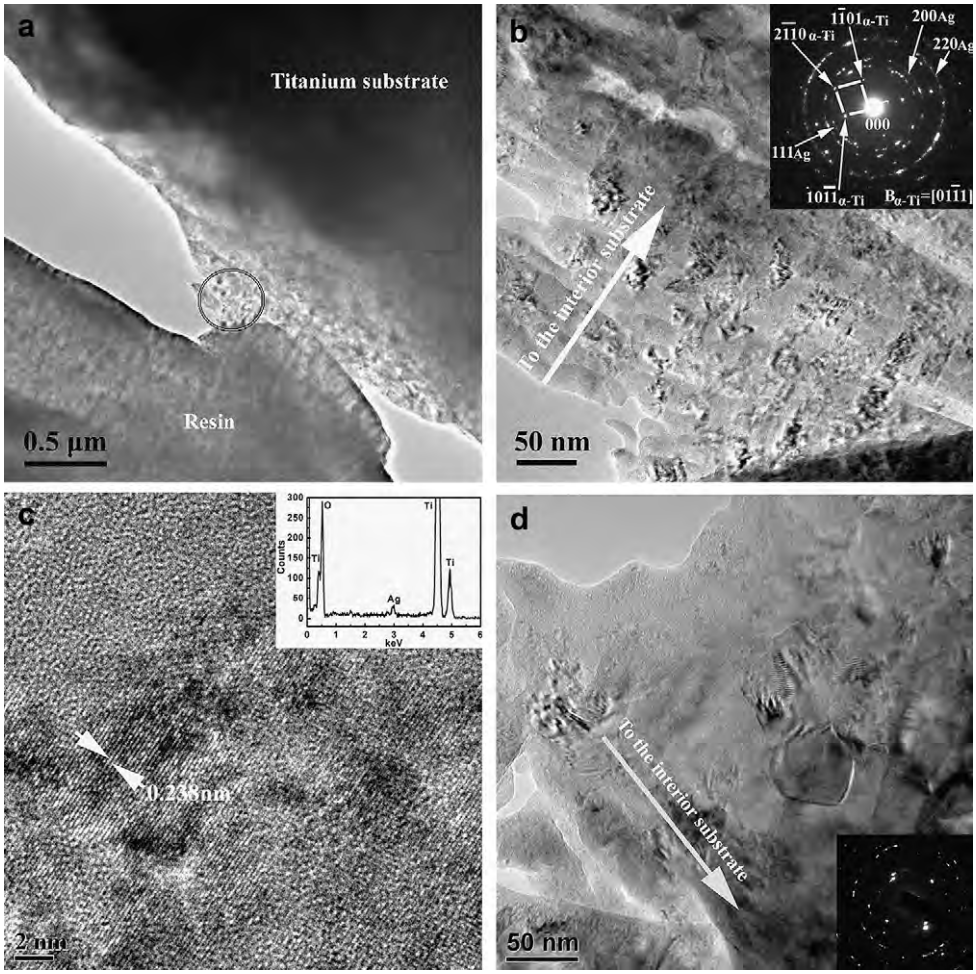

Fig. 2. TEM images for the Ag-PIII samples: (a) BF image acquired from 1.5h-Ag-PIII at low magnification, (b) BF image acquired from 1.5h-Ag-PIII at high magnification, (c) HR-TEM image of 1.5h-Ag-PIII, and (d) BF image of 1.0h-Ag-PIII. The insert in (b) and (d) are the corresponding SADP and the insert in (c) is the corresponding EDS spectrum.

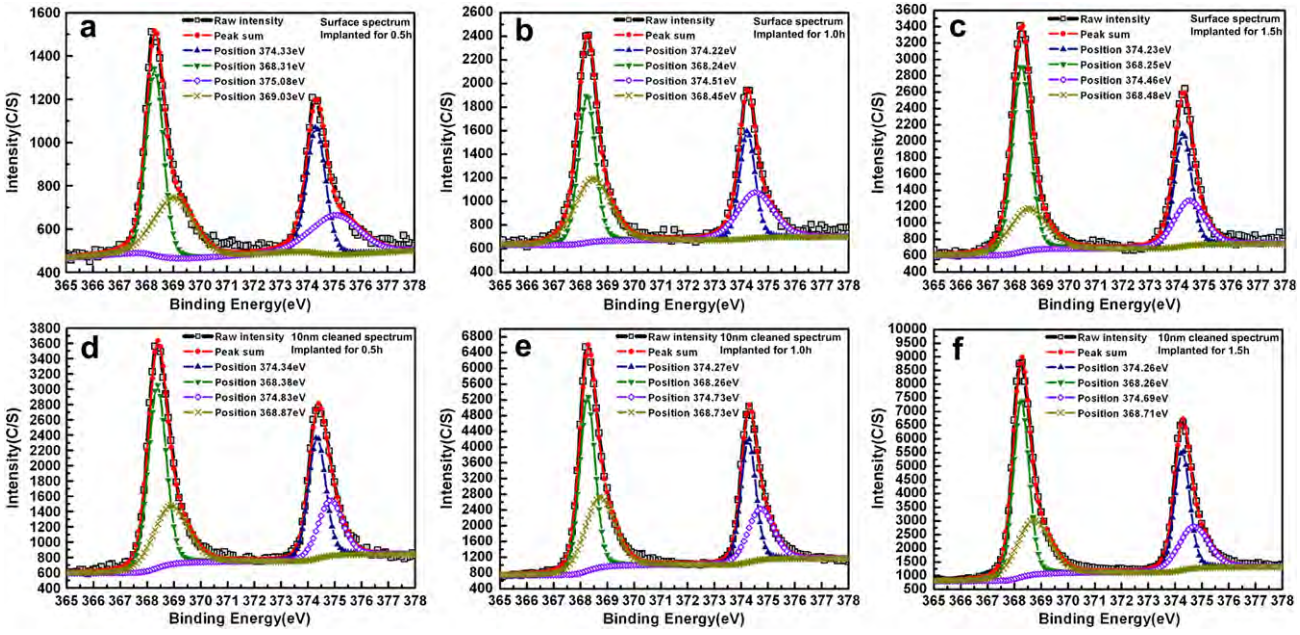

Fig. 3. Ag 3d XPS spectra obtained from the surface: (a) 0.5h-Ag-PIII, (b) 1.0h-Ag-PIII, and (c) 1.5h-Ag-PIII and spectra taken at a depth of 10 nm: (d) 0.5h-Ag-PIII, (e) 1.0h-Ag-PIII, and (f) 1.5h-Ag-PIII.

The XPS depth profiles in Fig. 4 are plotted on a depth scale based on a sputtering rate calculated from a SiO_2 reference under similar conditions. Since it is well known that the Ti sputtering rate changes in the surface region and is different from that of SiO_2, the depths are approximate, but comparison among different samples is more accurate. The amount of Ag increases with implantation time and the Ag depth profile obtained from 0.5h-Ag-PIII resembles a Gaussian distribution. The Ag peak (about 8 at.%) is located at about 30 nm. As the implantation time is increased to 1 h, the peak broadened towards the surface and the concentration increases slightly to about 10 at. %. The depth profile obtained from 1.5h-Ag-PIII is similar to that of 1.0h-Ag-PIII. Compared to 1.0h-Ag-PIII, the Ag distribution does not change, but the amount of Ag increases to about 12 at.%. The results indicate that the retained dose cannot be increased by simply increasing the implantation time due to sputtering. Although metallic silver cannot precipitate at such a concentration as suggested by the equilibrium phase diagram of Ti–Ag [26], Ag NPs form because of the non-equilibrium condition resulting from low (room) temperature implantation which limits the motility of silver atoms and produces local thermal spikes promoting precipitation of metallic silver particles and other interphases (such as Ti_2Ag, TiAg) from the solid solution of α-Ti(Ag) [27,28]. The chemical shift in the Ag3d peaks in Fig. 3 is likely because of the thermal spikes which induce the formation of solid solution of α-Ti (Ag), metallic silver particles, and other interphases during ion implantation and it is similar to that observed from magnesium alloys undergoing silver ion implantation [27,29].

The electrical charges on the surface are one of the main factors affecting the evolution of tissues around the implant [30] and so the zeta potentials are measured from the Cp Ti and Ag-PIII samples. Fig. 5 presents the average zeta potentials calculated from 20 measurements before and after Ag-PIII. They vary with the pH in the sodium chloride solution and are negative at the investigated pH values. The potentials on all the Ag-PIII samples are significantly less negative than that of the control Cp Ti at a pH of 7.0. In particular, the zeta potential on 0.5h-Ag-PIII is more negative than that on 1.5h-Ag-PIII but less negative than that on 1.0h-Ag-PIII. As shown in Fig. 5, the zeta potentials of the 0.5h-, 1.0h-, and 1.5h-Ag-PIII samples at a pH of 7.0 are −84.5 mV, −93.5 mV, and −60.1 mV respectively.

The change in the zeta potential pattern is likely related to the unique microstructure and electrochemical properties of the Ag NPs embedded titanium. Micro-galvanic couples between the Ag NPs and titanium matrix may be formed in the near surface. In order to evaluate the micro-galvanic efficiency, dynamic potential polarization

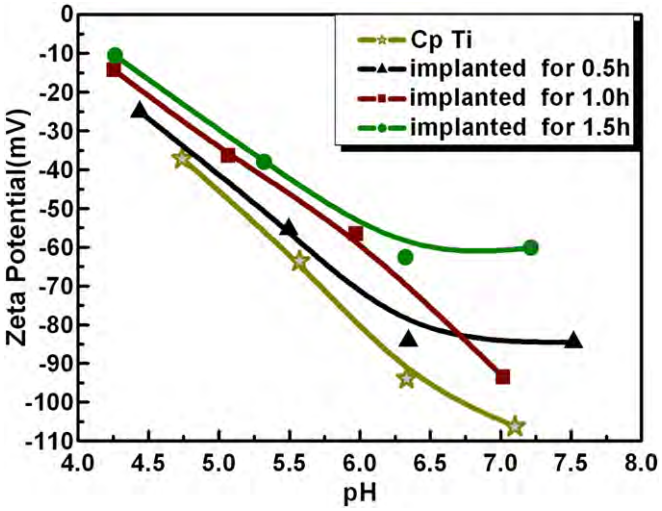

Fig. 5. Zeta potential variation versus pH of the sodium chloride solution acquired from the Cp Ti and Ag-PIII samples.

tests are conducted in a 0.9% NaCl solution (pH = 7.0). The Tafel plots and resulting data are exhibited in Fig. 6 and Table 2. The corrosion potentials (E_{cor}) measured from the 0.5h- and 1.0h-Ag-PIII samples shift a little negatively compared to the Cp Ti control, and a more notable shift is observed from 1.5h-Ag-PIII. As shown in Table 2, the corrosion potentials (E_{cor}) are about −479 mV, −572 mV, −0.583 mV, and −744 mV for CP–Ti and 0.5h, 1.0h and 1.5h-Ag-PIII. Besides, the corresponding corrosion current (I_{cor}) also increases slightly when the implantation time is lengthened from 0.5 to 1.5 h. It is likely related to the difference in the activation path between the micro-galvanic couples in the Ag NPs embedded titanium samples. Activation of the micro-galvanic couples is rapid on the surface when the sample is immersed in a solution, but activation of the micro-galvanic couples beneath the surface is slower and controlled by the lattice defect density in the near surface. The lattice defects caused by ion implantation provide fast diffusion paths for chloride ions (Cl^-) from the solution and facilitate activation of the micro-galvanic couples underneath. As shown by the TEM results, the lattice distortion intensity observed from 1.5h-Ag-PIII (Fig. 2c) is more serious than that detected from 1.0h-Ag-PIII (Fig. 2d). Hence, although the amount of Ag NPs on 1.5h-Ag-PIII is reduced (Fig. 1c), the shift observed

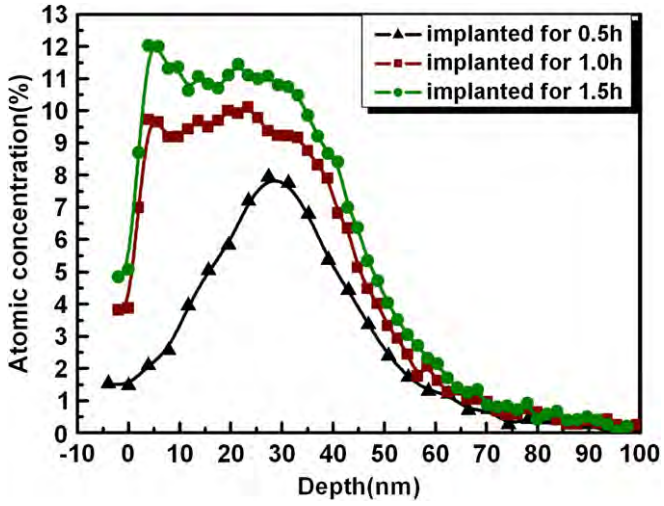

Fig. 4. Silver depth profiles.

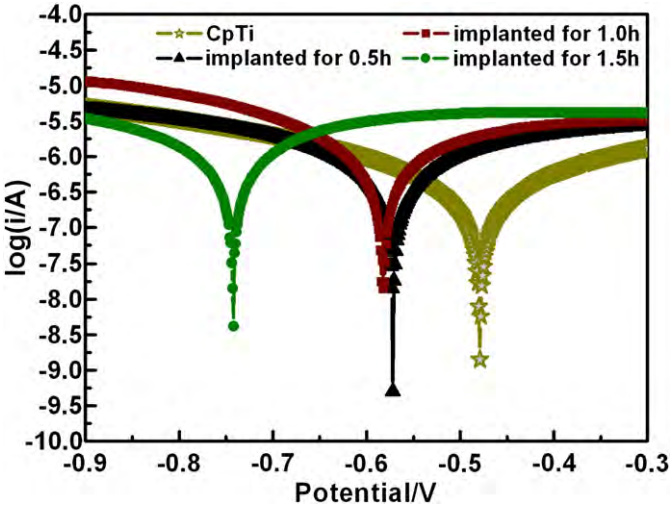

Fig. 6. Polarization curves.

Table 2
Parameters obtained by the Tafel polarization method.

	CpTi	0.5h-Ag-PIII	1.0h-Ag-PIII	1.5h-Ag-PIII
I_{cor} (A cm^{-2})	0.92E-6	1.19E-6	1.76E-6	2.18E-6
E_{cor} (mV) vs. SCE	−479	−572	−583	−744

from 1.5h-Ag-PIII can still be detected due to activation of the micro-galvanic couples underneath via these lattice defect paths. The results indicate that the micro-galvanic effects exist on and underneath the Ag-PIII surfaces, and activation of the effect, which is more difficult beneath the surface, is related to the lattice defects and Ag-PIII time (a longer implantation time means more nuclear collisions). This effect may further influence the zeta potentials on the Ag-PIII samples and the relationship between the zeta potentials and micro-galvanic effects will be discussed further in the discussion section.

3.2. Response of cells to the Ag-PIII surfaces

3.2.1. Effects on bacteria

The morphology of the bacteria (*S. aureus* and *E. coli* species) seeded on both the Cp Ti and the Ag-PIII surfaces are observed by

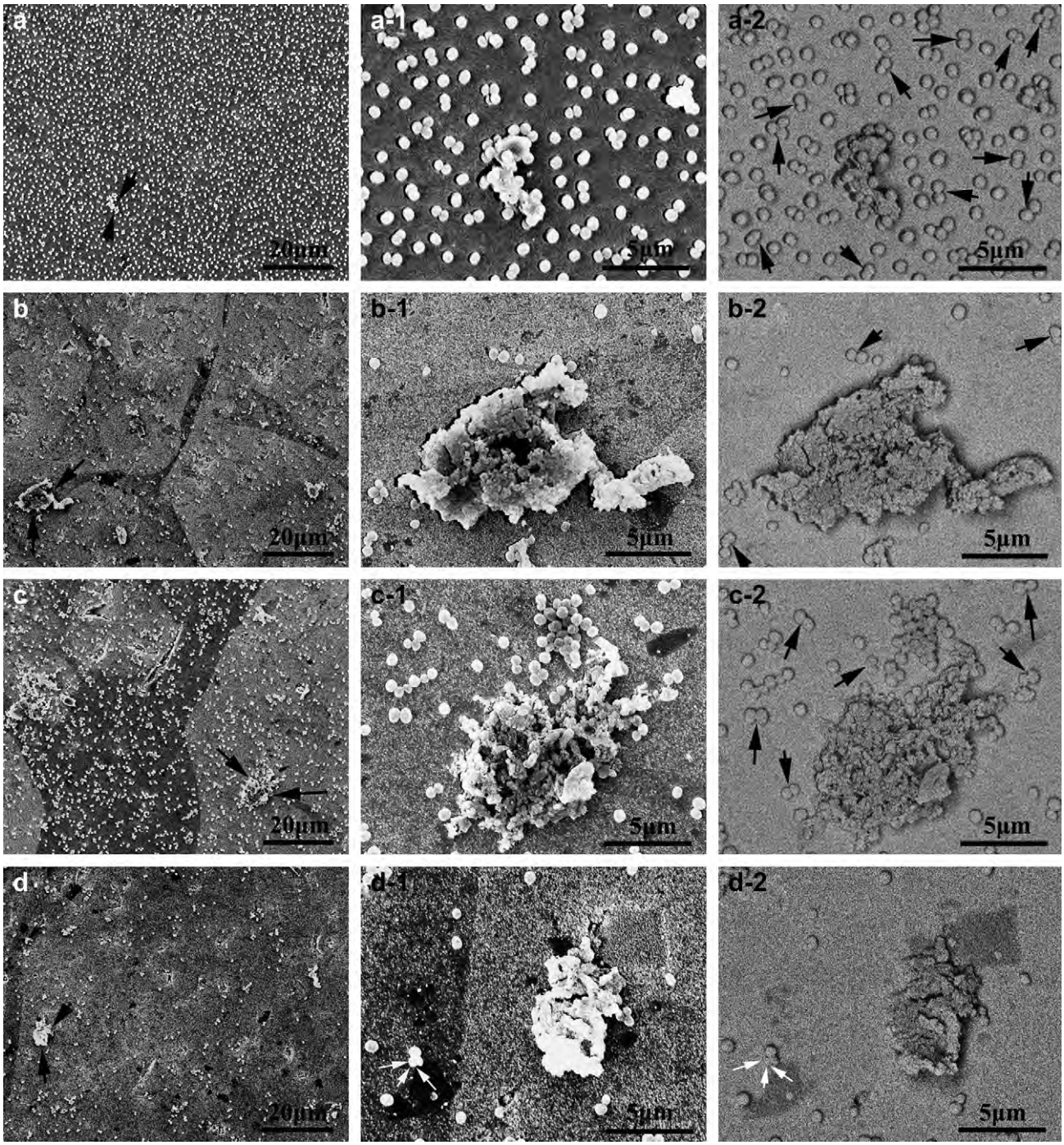

Fig. 7. SEM morphology of the *S. aureus* species seeded on the various surfaces SEI images at (i) low magnification and (i-1) and high magnification together with (i-2) the corresponding BES image [i = a, b, c, and d represent Cp Ti, 0.5h-Ag-PIII, 1.0h-Ag-PIII, and 1.5h-Ag-PIII, respectively and the bacteria concentration is 10^8 cfu/ml].

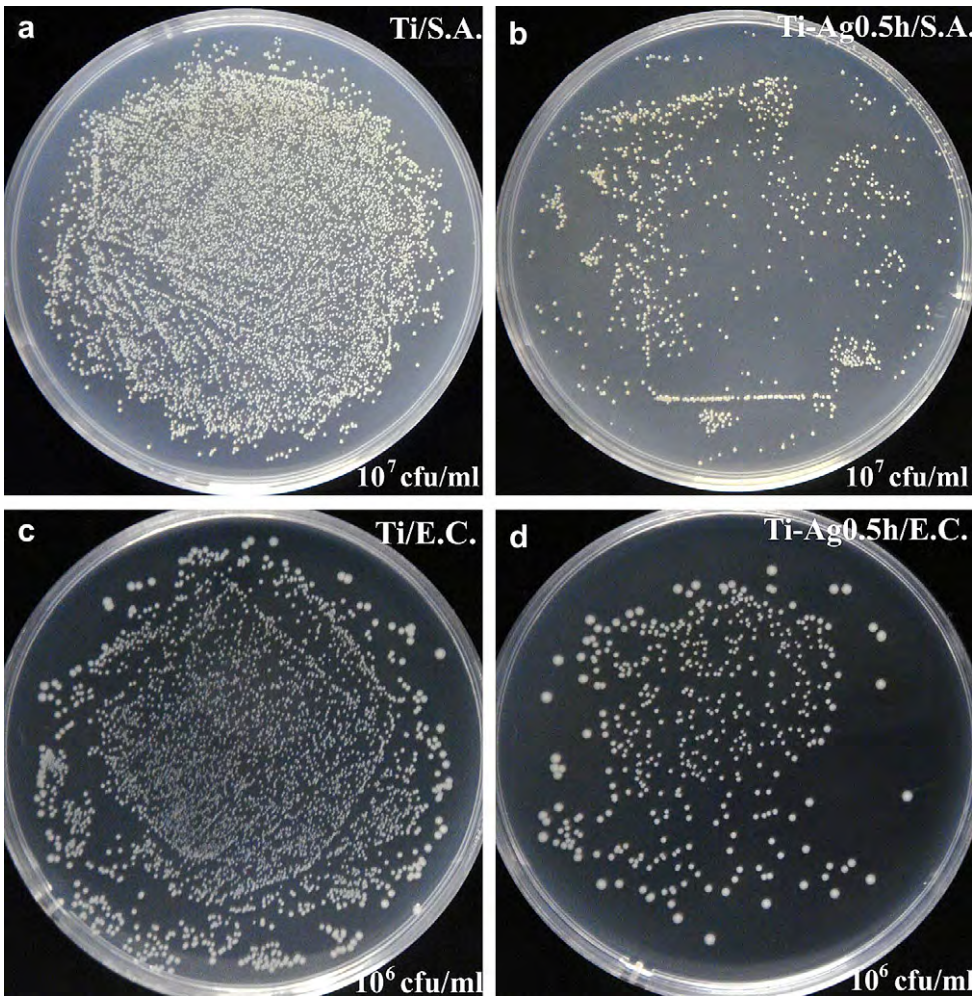

Fig. 8. Re-cultivated bacterial colonies on agar: *S. aureus* colonies are previous dissociated from (a) Cp Ti, (b) 0.5h-Ag-PIII with the re-cultivated bacteria concentration being 10^7 cfu/ml. The *E. coli* colonies are previous dissociated from (c) Cp Ti and (d) 0.5h-Ag-PIII with re-cultivated bacteria concentration being 10^6 cfu/ml.

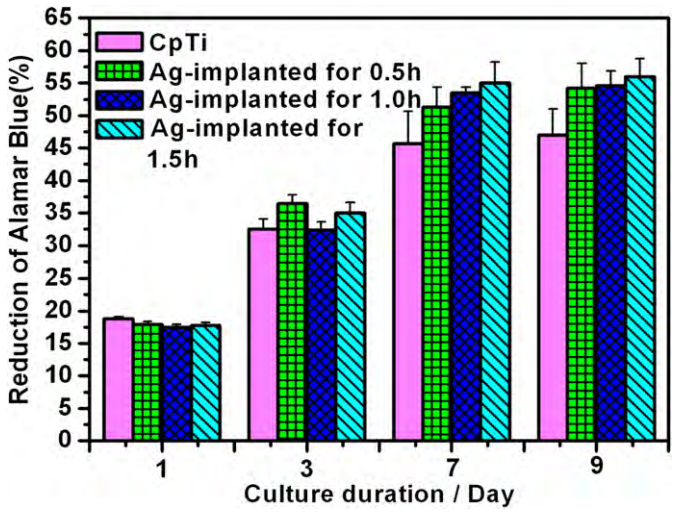

Fig. 9. Reduction percentage of alamarBlue™ for MG63 cells cultured for various periods of time on the various surfaces [cell density in the suspension is 1×10^5 cell/ml].

SEM. Both the secondary electron (SEI) and backscattered electron (BES) signals are utilized to identify the shape and membrane integrity. Cell division predominates on Cp Ti surface but not on the Ag-PIII samples, indicating that the Ag-PIII surfaces are cytostatic or cytocidal to the bacteria. Fig. 7 depicts the typical SEM images of *S. aureus* on both the Cp Ti and Ag-PIII samples. The attached cell density measured on Cp Ti, 0.5h-Ag-PIII, 1.0h-Ag-PIII, and 1.5h-Ag-PIII are 3.3×10^5, 8.1×10^4, 1.7×10^5, and 4.6×10^4 cells/mm^2. The evolution pattern is in consistent with that of the zeta potential at the pH of 7.0 (Fig. 6), indicating that bacteria attachment correlates with the surface zeta potential change. Binary or multiple fission (black arrow in Fig. 7a-2) is often observed but not small dead-cell colonies (black arrow in Fig. 7a), whereas more large dead-cell colonies (black arrow in Fig. 7b, c, and d) and small amount of fission (black arrow in Fig. 7b-2 and c-2) are observed on the Ag-PIII surfaces, implying that *S. aureus* can grow well and rapidly on Cp Ti but can hardly survive on the Ag-PIII surfaces. Besides, although the shape of some cells are found on the Ag-PIII surfaces, the membrane contrast (see the backscattered electron images in Fig. 7b-2, c-2, and d-2) is not as sharp as that on Cp Ti (Fig. 7a-2) and some of them even merge with the background (white arrow in Fig. 7d-1 and d-2). The results show that death of the bacteria on the Ag-PIII samples is likely due to the disruption of the bacterial membrane integrity.

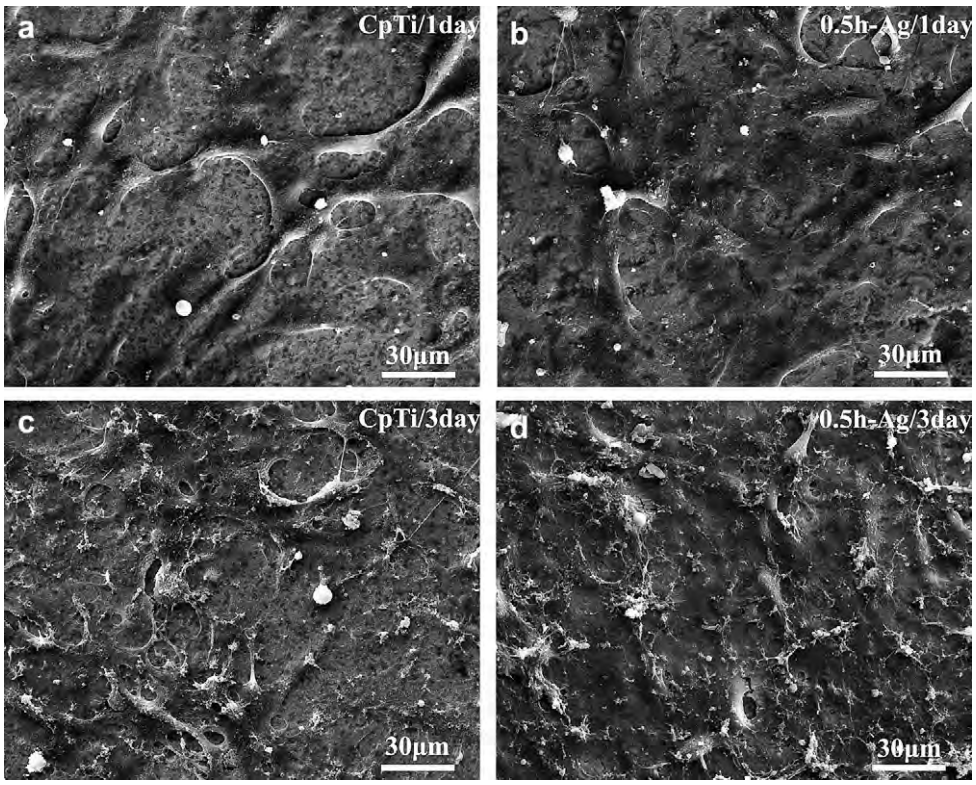

Fig. 10. SEM morphology of the MG63 cells cultured on Cp Ti after: (a) 1 day and (c) 3 days and on 0.5h-Ag-PIII after: (b) 1 day and (d) 3 days [cell density in the suspension is 1×10^5 cell/ml].

To determine the bacteriostatic or bactericidal effect on the Ag-PIII samples, the attached bacteria are dissociated off the surfaces and re-cultivated on agar according to the bacteria counting method. The results indicate that all the Ag-PIII surfaces are able to reduce the proliferation of both types of bacteria. Fig. 8 shows the typical photos of the number of bacteria colonies on Cp Ti and 0.5h-Ag-PIII. The amounts of *S. aureus* and *E. coli* on 0.5h-Ag-PIII are reduced by approximately 93% and 95% after 24 h. The amount of silver released from the Ag-PIII samples are determined by ICP-OES, and less than a 10 ppb Ag^+ is found in water at 37 °C even after 60 days, indicating that leaching of Ag^+ from the NPs is minimal. It is generally accepted that the antibacterial action of Ag NPs depends on the availability of silver ions [6]. Other studies have shown that oxidizing species in lieu of reducing agents are responsible for the antibacterial effects [31]. The extremely low silver concentration in the solution rules out the inherent toxicity of Ag^+ to bacteria and so the inhibition to bacteria is mainly due to metallic (Ag^0) rather than Ag^+ released from the Ag NPs. The underlying factors contributing to the antimicrobial results may be similar to that of the silver and clay nanohybrids observed by Su et al. [32] that the nanohybrids of silver and clay can induce bacteria death merely through physical contact. The bacteriostatic and bactericidal properties of the Ag-PIII samples will be discussed further in the next section.

3.2.2. Response of osteoblast-like cell line MG63

The proliferation and vitality of MG63 cells cultured on the Cp Ti and Ag-PIII samples are determined by using the alamarBlue™ assay and the results are shown in Fig. 9. Cell proliferation on all the Ag-PIII surfaces is slightly lower than that on Cp Ti after culturing for 1 day. However, after culturing for 3, 7, and 9 days, the cells on all the Ag-PIII samples show higher proliferation rates and viability than those on Cp Ti, indicating that Ag PIII introduces very little adverse or even more favorable effects on osteoblast proliferation. The cell morphologies on Cp Ti and 0.5h-Ag-PIII after culturing for 1 and 3 days are depicted in Fig. 10. The individual and clustered osteoblasts cover both surfaces and complete cell spreading is also observed. The *in vitro* cell culture assay reveals no significant cytotoxicity and even good cytocompatibility on the Ag-PIII samples. The good cytocompatibility on the Ag-PIII surfaces may be related to the surface micro-galvanic couples which promote aggregation of proton (H^+) surrounding the Ag NPs. The mechanism will be discussed in the discussion section.

To explore the initial (within the first hours) cell adherence process, the cytoskeleton of the osteoblast-like MG63 cells seeded on the both surfaces are examined by laser scanning confocal microscopy (LSCM) after staining with phalloidin, anti-vinculin, and DAPI to visualize the filamentous F-actin, vinculin expression, and cell nuclei, respectively. The results are presented in Figs. 11and 12. Although the cells on all the surfaces exhibit a round morphology (Fig. 11a-1, b-1, c-1, and d-1) in the first hour, the expression of filamentous F-actin on the Ag-PIII samples is a little lower than that on Cp Ti surface. Mitosis phase cells can be observed on Cp Ti within 3 h (white arrow in Fig. 11a-2), whereas cells in the mitosis phase can hardly be detected on the Ag-PIII surfaces until after incubation for 5 h (white arrow in Fig. 11b-3, c-3, and d-3), indicating that the Cp Ti surface is more preferable than that on the Ag-PIII samples in the initial stage of cell adhesion. The data are consistent with the results presented in Fig. 9 which shows that the proliferation rates on all the Ag-PIII samples are slightly lower than that on Cp Ti after 1 day. However, there is no obvious difference in the filamentous F-actin expression after 5 h, and after culturing for 24 h, the cells on all the samples show a multi-polar spindle morphology with a well-organized cytoskeleton structure (Fig. 11a-4, b-4, c-4 and d-4), suggesting that the cells acclimate rapidly to the surfaces, and silver

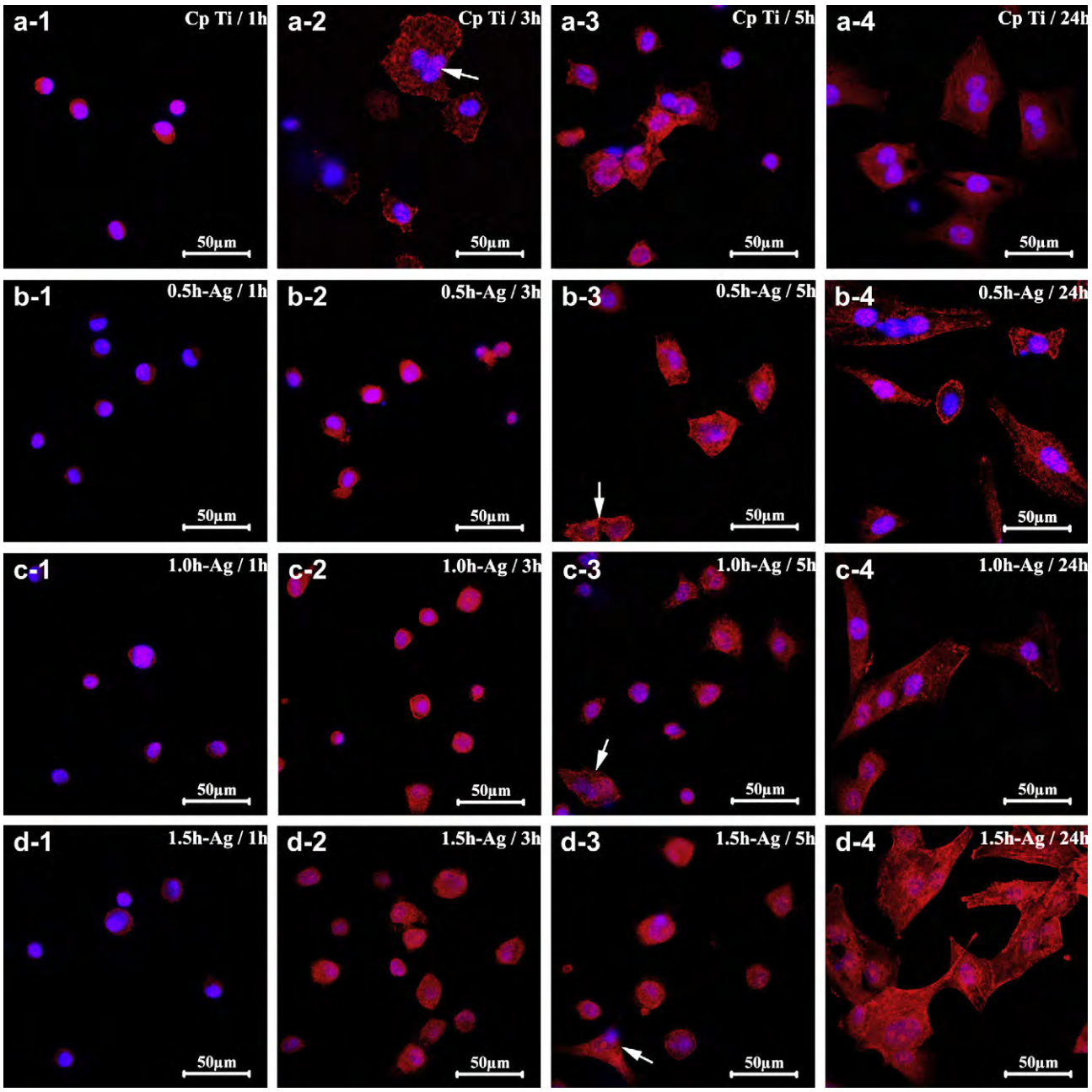

Fig. 11. LSCM images of MG63 cells cultured for 1 h (i-1), 3 h (i-2), 5 h (i-3), and 24 h (i-4)on the various surfaces with F-actin stained with rhodamine phalloidin (red) and the nucleus stained with DAPI (blue) at a cell density in the suspension of 1×10^4 cell/ml [i = a, b, c and d represent Cp Ti, 0.5h-Ag-PIII, 1.0h-Ag-PIII, and 1.5h-Ag-PIII, respectively].

has very little effects on cell proliferation. This is likely due to the restricted mobility of embedded Ag NPs which exclude their uptake through endocytosis and macropinocytosis. The uptake of Ag NPs may inhibit cell proliferation [33]. Moreover, the expression of focal adhesion protein vinculin on the Ag-PIII samples is remarkably lower than that on Cp Ti in the first hour, especially that on 1.0h-Ag-PIII (white arrow in Fig. 12c-1). This difference cannot be observed if the culture time exceeds 3 h, indicating that the Ag NPs only impact the initial gravitation/sedimentation stage during cell attachment. The surface wetting characteristics are important to cell adhesion which is generally better on a hydrophilic surface [34]. This because cells adhere by binding to the adsorbed adhesion ligands and the adsorption of adhesion ligand depends on the surface wettability which determines the conformation of proteins [35]. In the present study, the contact angles measured from the Cp Ti and Ag-PIII surfaces are 71 ± 1 and $107 \pm 1^\circ$, respectively. The Ag-PIII surface is thus more hydrophobic than that of Cp Ti. Therefore, the difference in the cell proliferation and attachment in the initial stage may be a direct consequence of the difference in the surface wettability.

4. Discussion

The Ag NPs are embedded in titanium by one-step silver plasma immersion ion implantation (Ag-PIII). As discussed in the previous section, the Ag NPs are formed via a local nucleation process and show efficient antibacterial activity and good cytocompatibility. At the same time, leaching of silver ions from the sample surface is not severe. Many studies have shown that silver is toxic at high concentrations [36] and it has also been shown that Ag NPs are cytotoxic to mitochondrial or liver cells [37], but the exact

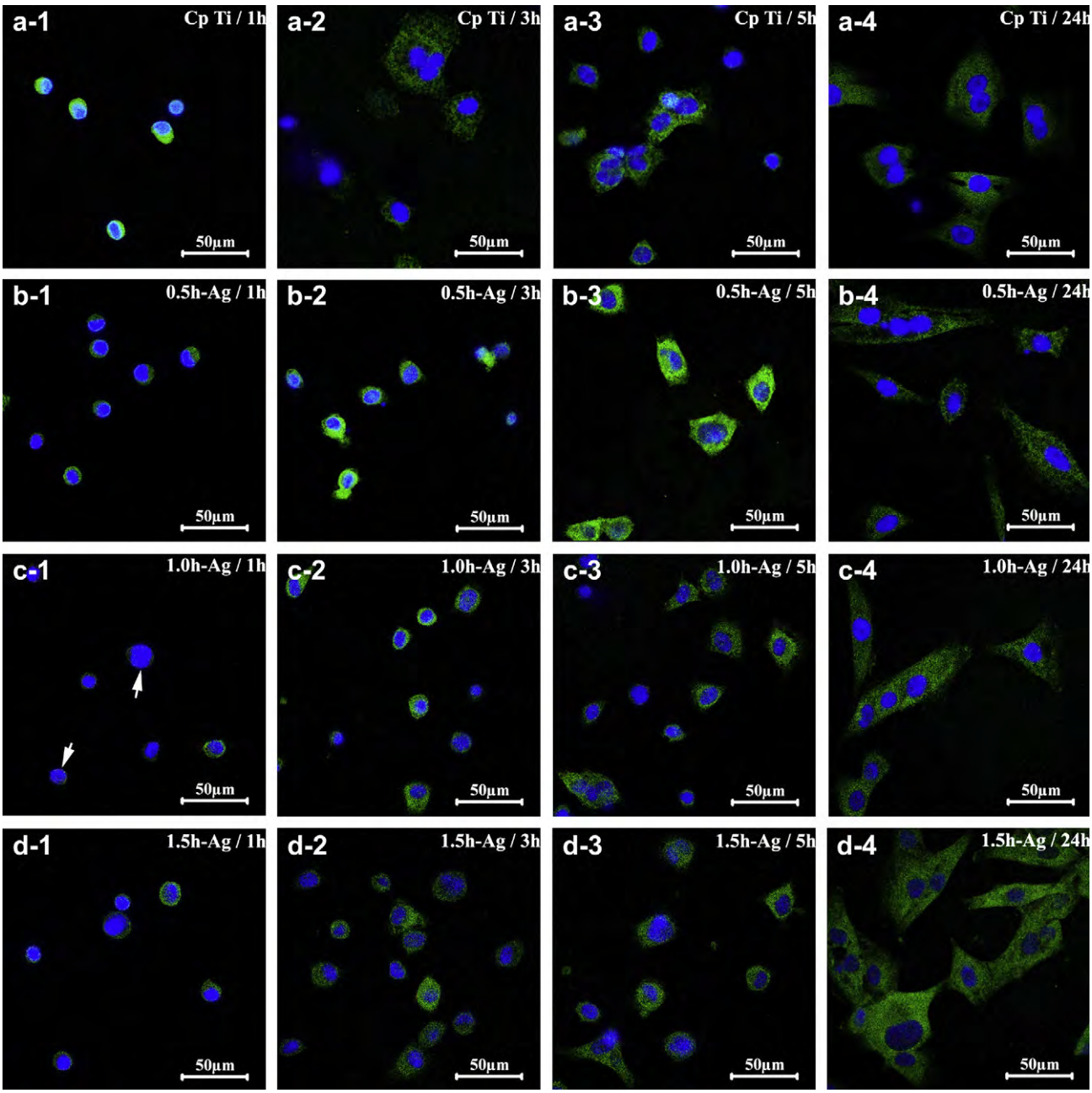

Fig. 12. LSCM images of MG63 cells cultured for 1 h (i-1), 3 h (i-2), 5 h (i-3), and 24 h (i-4) on the various surfaces with vinculin stained with anti-vinculin (green) and the nucleus stained with DAPI (blue) at a cell density in the suspension of 1×10^4 cell/ml [i = a, b, c, and d represent Cp Ti, 0.5h-Ag-PIII, 1.0h-Ag-PIII, and 1.5h-Ag-PIII, respectively].

mechanism is still not well understood. It has been suggested that Ag NPs are toxic because of out-leaching of silver ions and Ag NPs alone are not a direct source of toxicity [38]. Other studies have suggested that Ag NPs are cytotoxic because of the oxidative stress that is independent of the toxicity of silver ions [14]. Nonetheless, although it is reasonable to assume that the physico-chemical characteristics of Ag NPs determine their potential cytotoxicity, these properties have not been investigated in details [18]. In this study, on account of the absence of other stabilizers, the micro-galvanic effects can be easily triggered when the Ag NPs embedded titanium is immersed in a physiological liquid, as shown in Fig. 13. The micro-galvanic effect stems from the micro-galvanic couples between the Ag NPs and titanium substrate due to the fact that the standard electrode potential of titanium (Ti) which is $E^{\circ}_{Ti} = -1.630$ V is markedly more negative than that of silver that is $E^{\circ}_{Ag} = 0.7996$ V [39]. The galvanic corrosion rate of a single mico-galvanic couple is basically determined by its galvanic current [40], I_g, which can be theoretically expressed as [41]:

$$I_g = (E_c - E_a)/(R_a + R_c + R_s + R_m) \quad (2)$$

where I_g is the galvanic current between the anode and cathode, E_c and E_a are the open circuit potentials of the cathode and anode respectively, and R_c, R_a, R_s, and R_m are the resistances corresponding to the cathode, anode, solution path between the anode and cathode, and metallic path from the anode surface to the cathode surface.

The embedded Ag NP microstructure provides the basic components for the micro-galvanic couples. That is, the embedded Ag NPs act as the cathode and the α-Ti matrix serves as the anode. However, according to Equation (2), the micro-galvanic couples are not activated until they are immersed in a liquid when the cathodes

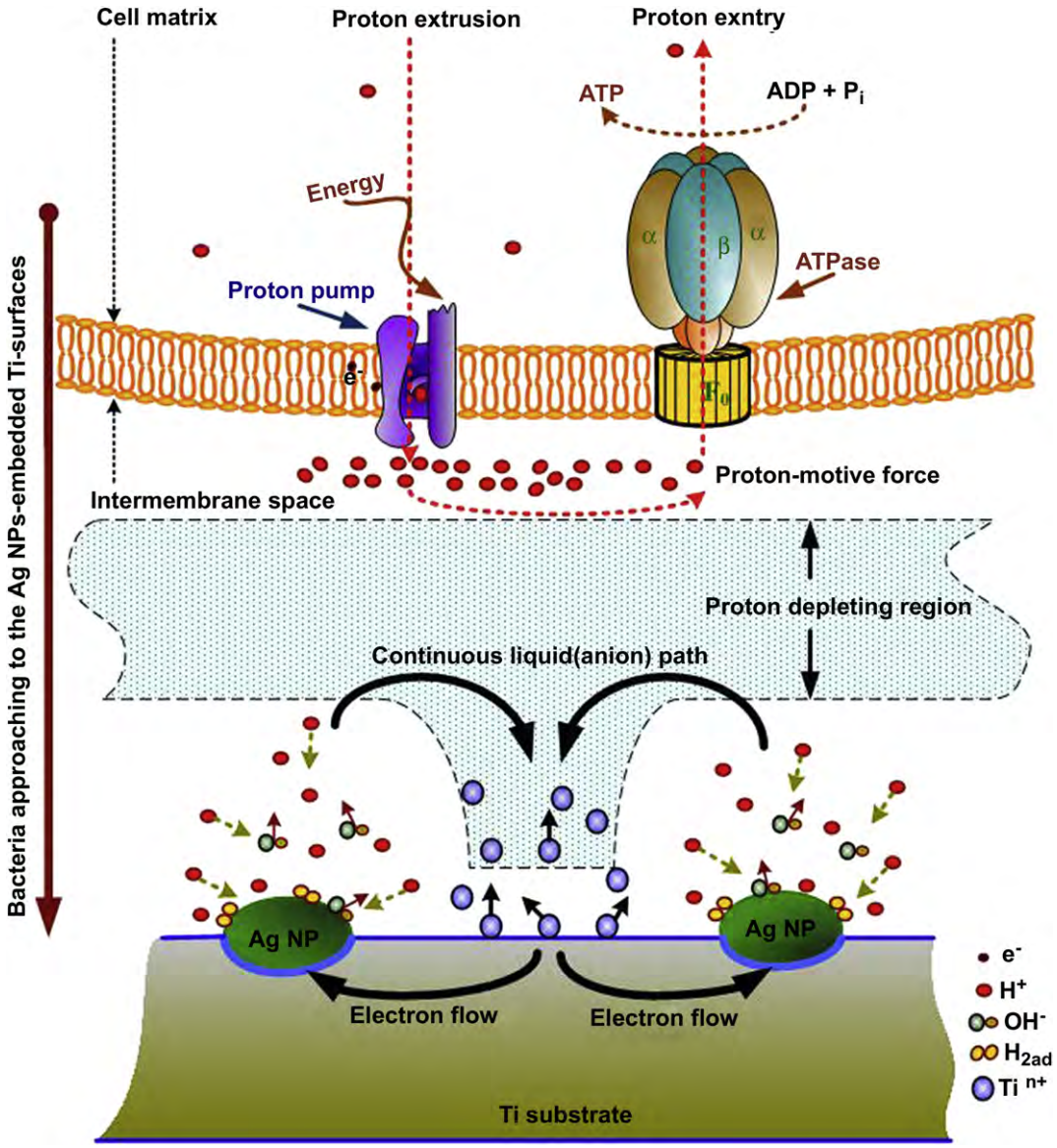

Fig. 13. Illustration for the possible toxicity mechanism on the Ag NPs embedded surfaces.

and anode are in a conducting state (activation). Moreover, the ions in the solution path and near the surface lattice defects control the activation rate. Therefore, the efficiency of those micro-galvanic couples is determined by the amount of embedded Ag NPs which determine the overall galvanic current and the lattice defects which control the activation of the couples underneath the surface. This is verified by the Tafel plots of the Ag-PIII samples in Fig. 6. In the present circumstances, the anodic reaction occurs according to equation (3):

$$\mathrm{Ti} \rightarrow \mathrm{Ti}^{n+} + ne^{-} \tag{3}$$

Titanium ions (Ti^{n+}) pass into the surrounding solution (cell culture medium) and electrons (ne^{-}) are transported from the titanium matrix to the Ag NPs where these electrons are consumed by the cathodic reaction. There are two different cathodic reactions depending on the availability of oxygen and the pH of the solution: (a) evolution of hydrogen from the acidic or neutral medium according to reactions (4) and (5) [42,43], and (b) reduction of the dissolved oxygen gas in the acidic or neutral solutions according to reactions (6) and (7) [44,45]:

$$2\mathrm{H}^{+} + 2\mathrm{e}^{-} \rightarrow \mathrm{H}_2 (pH < 7.0) \tag{4}$$

$$2\mathrm{H}_2\mathrm{O} + 2\mathrm{e}^{-} \rightarrow \mathrm{H}_2 + 2\mathrm{OH}^{-} (pH \geq 7.0) \tag{5}$$

$$\mathrm{O}_2 + 4\mathrm{H}^{+} + 4\mathrm{e}^{-} \rightarrow 2\mathrm{H}_2\mathrm{O} (pH < 7.0) \tag{6}$$

$$\mathrm{O}_2 + 2\mathrm{H}_2\mathrm{O} + 4\mathrm{e}^{-} \rightarrow 4\mathrm{OH}^{-} (pH \geq 7.0) \tag{7}$$

hence, in the acidic solution, reactions (4) and (6) predominate in the cathodic reaction whereas in a neutral or basic solution, reactions (5) and (7) occur primarily. Protons (H^{+} involved in the cathodic reactions) and chloride ions (Cl^{-} involved in the anodic reaction) are the two main charged species in the solution path influencing the activation and efficiency of the micro-galvanic couples. Since there are enough protons in the acidic solutions for reactions (4) and (6), stable titanium ions release results via reaction (3). The positively charged titanium ions may affect the status of the electrical double layer on the Ag-PIII surface and degrade the negatively charged titanium surface so that positive particles are

Table 3
Diffusion coefficients (D) [46] and effective ionic radius (IR) [47] of the involved ions.

Ions	IR (Angstroms)	D ($10^{-5}cm^2s^{-1}$)
Cl^-	1.81	2.032
Na^+	0.99	1.334
H^+	−0.38	9.311
OH^-	1.32	5.273

attracted from the test solution. This is responsible for the steady shift in the zeta potentials to being less negative in the pH range from 4.0 to 6.5 on 1.0h-Ag-PIII (Fig. 5). As the pH increases, the zeta potential shift changes gradually and when the pH value exceeds 6.7, 1.0h-Ag-PIII becomes the most negative among the three Ag-PIII samples (Fig. 5). This is likely because reactions (5) and (7) dominate the cathodic reactions due to the lack of protons in the basic medium and anodic reaction (3), that is, chlorine ions controlling the activation of the micro-galvanic couples beneath the surface. Furthermore, as shown in Table 3, the diffusion coefficient of chloride ions is about one fifth of that of protons [46] and the ionic radius of chloride ions is about 5 times larger than that of protons [47]. Hence, it is more difficult for chloride ions to diffuse along the low density lattice defect paths to activate the micro-galvanic couples below the surface in 1.0h-Ag-PIII. It is in conjunction with the particle density decrease on the surface resulting in the lower overall micro-galvanic efficiency on 1.0h-Ag-PIII than 0.5h-Ag-PIII. Although reactions (5) and (7) are more likely involved here because of the neutral or weak basic nature of the cell culture (pH of 7.0 or 7.4), the local cathodic reactions described by equations (4) and (6) cannot be excluded when acidic extracellular species are involved in cell adhesion [48]. Reactions (4) and (6) consume protons and because the diffusion coefficient of H^+ is $9.311E^{-5}$ cm^2s^{-1} which is about twice that of OH^- ($5.273E^{-5}$ cm^2s^{-1}) (Table 3), OH^- produced from reactions (5) and (7) can further react with protons to form water adjacent to the Ag NPs. Therefore, as shown by Fig. 13, proton depleted regions are likely formed around the Ag NPs embedded surface due to proton consumption described by reactions (4)–(7).

The proton depleted regions may disrupt the proton electrochemical gradient in the intermembrane space of the bacteria and interfere with adhesion and proliferation. The proton electrochemical gradient is established by the respiration process of the electron transport chain embedded on the cell membrane which leads to the net transfer of protons from the inside to the outside of the bacteria. When protons migrate down the electrochemical gradient and enter the cell via the ATPase, adenosine triphosphate (ATP) synthesis occurs. Hence, the electrochemical potential of protons provides the driving force for the ATP synthesis in the mitochondria and most bacteria [49]. The ATP serves as a general energy source for all living cells [50] and the proton electrochemical gradient is essential to maintaining the energy-dependent reactions in the bacteria. The disruption of the transmembrane proton electrochemical gradient may inactivate the ATP synthesis, ion transport, and metabolite sequestration [51], ultimately lead the cell death. It is thus believed that the proton depleted regions resulting from the cathodic reactions disrupts the transmembrane proton electrochemical gradient which is responsible for the death of both *S. aureus* and *E. coli* seeded on the Ag NPs embedded titanium surfaces. This postulated mechanism is consistent with the proteomic analysis results which indicate that Ag NPs may accumulate in the protein precursors leading to depleted intracellular ATP levels [52]. However, the responses of the bacteria and osteoblast-like MG63 cells are obviously different in the present study. Proliferation of bacteria is inhibited (Fig. 7) whereas that of osteoblasts is promoted (Fig. 9). The difference is likely due to the difference in size and structure between the prokaryotic (bacteria cells) and eukaryotic cells (MG 63 cells). Eukaryotic cells are normally much bigger than prokaryotic cells. More important, the mitochondria serve as the main organelles in the production of adenosine triphosphate (ATP) for the eukaryotic cells [53]. They are membrane-bounded into a more complex endomembrane system [54] but the prokaryotic cells are not. Hence, the limited size of the proton depleted regions cannot affect the overall proton electrochemical gradient of a eukaryotic cell and interfere with the synthesis of ATP. On the contrary, the aggregated proton adjacent to the Ag-PIII surface may promote the overall energy-dependent reactions and proliferation on the macroscopic scale because of the larger size. Hence, the biological activities on the Ag NPs embedded titanium surface can be manipulated by the micro-galvanic effect resulting from the electrochemical properties of silver and titanium. Although the postulate illustrated in Fig. 13 explains to some extent the mechanism, the specific processes require more in-depth studies, but nevertheless, the present study provides new insights to the application of Ag NPs and the associated activity.

5. Conclusion

Ag NPs are embedded in titanium by a one-step silver plasma immersion ion implantation process. The nanoparticles precipitate on and underneath the titanium surface via a local nucleation process in the solid solution of α-Ti(Ag). The embedded samples are highly effective in inhibiting both *S. aureus* and *E. coli* strains while exhibit obvious activity in promoting proliferation of the osteoblast-like cell line MG63. The micro-galvanic couples formed by the Ag NPs and Ti matrix play an important role in the interactions with the attached cells. The physico-chemical characteristics of the Ag NPs are essential factors affecting the surface cytotoxicity and the present study provides new insights to the application of Ag NPs and the associated activity.

Acknowledgments

This work was jointly supported by Shanghai Science and Technology R&D Fund under grant 0952nm04400, National Natural Science Foundation of China No.30700170 and No.51071168, Shanghai Post Doctoral Science Research Fund under grant No.10R21416900, China Post Doctoral Science Foundation under grant No.20100470736, Shanghai-Unilever Research and Development Fund 09520715200, Innovation Fund of SICCAS under grant Y06ZC3130G, City University of Hong Kong Strategic Research Grant (SRG) No. 7008009, City University of Hong Kong matching research grant No. 9678021, and Hong Kong Research Grants Council (RGC) General Research Funds (GRF) Nos. CityU 112307 and 112510.

Appendix

Figures with essential color discrimination. Figs. 1, 3–6, 8, 9, 11–13 in this article are difficult to interpret in black and white. The full color images can be found in the on-line version, at doi:10.1016/j.biomaterials.2010.09.066

References

[1] Geetha M, Singh AK, Asokamani R, Gogia AK. Ti based biomaterials, the ultimate choice for orthopaedic implants-a review. Prog Mater Sci 2009;54:397–425.
[2] Costerton JW, Stewart PS, Greenberg EP. Bacterial biofilms: a common cause of persistent infections. Science 1999;284:1318–22.
[3] Johannsson B, Callaghan JJ. Prosthetic hip infection due to *Cryptococcus neoformans*: case report. Diagn Micr Infec Dis 2009;64:76–9.

[4] Ochoa RAT, Mow CS. Deep infection of a total knee implant as a complication of disseminated *Pneumococcal sepsis*. a case report and review of literature. Knee 2008;15:144–7.
[5] Agarwal A, Weis TL, Schurr MJ, Faith NG, Czuprynski CJ, McAnulty JF, et al. Surfaces modified with nanometer-thick silver-impregnated polymeric films that kill bacteria but support growth of mammalian cells. Biomaterials 2010;31:680–90.
[6] Chen X, Schluesener HJ. Nanosilver: a nanoproduct in medical application. Toxicol Lett 2008;176:1–12.
[7] Li Z, Lee D, Sheng X, Cohen RE, Rubner MF. Two-level antibacterial coating with both release-killing and contact-killing capabilities. Langmuir 2006;22:9820–3.
[8] Yuan W, Ji J, Fu J, Shen J. A facile method to construct hybrid multilayered films as a strong and multifunctional antibacterial coating. J Biomed Mater Res B 2008;85:556–63.
[9] Vasilev K, Sah V, Anselme K, Ndi C, Mateescu M, Dollmann B, et al. Tunable antibacterial coatings that support mammalian cell growth. Nano Lett 2010;10:202–7.
[10] Morones JR, Elechiguerra JL, Camacho A, Holt K, Kouri JB, Ramírez JT, et al. The bactericidal effect of silver nanoparticles. Nanotechnology 2005;16:2346–53.
[11] Elechiguerra JL, Burt JL, Morones JR, Bragado AC, Gao X, Lara HH, et al. Interaction of silver nanoparticles with HIV-1. J Nanobiotechnology 2005;3:6.
[12] Pal S, Tak YK, Song JM. Does the antibacterial activity of silver nanoparticles depend on the shape of the nanoparticle? a study of the gram-negative bacterium *Escherichia coli*. Appl Environ Microbiol 2007;27:1712–20.
[13] Park EJ, Yi J, Kim Y, Choi K, Park K. Silver nanoparticles induce cytotoxicity by a Trojan-horse type mechanism. Toxicol In Vitro 2010;24:872–8.
[14] Kim S, Choi JE, Choi J, Chung K, Park K, Yi J, et al. Oxidative stress-dependent toxicity of silver nanoparticles in human hepatoma cells. Toxicol In Vitro 2009;23:1076–84.
[15] Sur I, Cam D, Kahraman M, Baysal A, Culha1 M. Interaction of multi-functional silver nanoparticles with living cells. Nanotechnology 2010;21:175104.
[16] Bois L, Chassagneux F, Battie Y, Bessueille F, Mollet L, Parola S, et al. Chemical growth and photochromism of silver nanoparticles into a mesoporous titania template. Langmuir 2010;26:1199–206.
[17] Barrena R, Casals E, Colón J, Font X, Sánchez A, Puntes V. Evaluation of the ecotoxicity of model nanoparticles. Chemosphere 2009;75:850–7.
[18] Kramer J, Bell R, Smith S, Gorsuch J. Silver nanoparticle tocicity and biocides: need for chemical speciation. Integr Environ Assess Manag 2009;5:720–2.
[19] Pelletier J, Anders A. Plasma-based ion implantation and deposition: a review of physics, technology, and applications. IEEE Trans Plasma Sci 2005;33:1–72.
[20] Huang N, Yang P, Leng YX, Wang J, Sun H, Chen JY, et al. Surface modification of biomaterials by plasma immersion ion implantation. Surf Coat Tech 2004;186:218–26.
[21] Monteiro DR, Gorup LF, Takamiya AS, Ruvollo-Filho AC, de Camargo ER, Barbosa DB. The growing importance of materials that prevent microbial adhesion: antimicrobial effect of medical devices containing silver. Int J Antimicrob Agents 2009;34:103–10.
[22] Zhang W, Luo Y, Wang H, Jiang J, Pu S, Chu PK. Ag and Ag/N_2 plasma modification of polyethylene for the enhancement of antibacterial properties and cell growth/proliferation. Acta Biomater 2008;4:2028–36.
[23] Zhang W, Luo Y, Wang H, Pu S, Chu PK. Biocompatibility of silver and copper plasma doped polyethylene. Surf Coat Tech 2009;203:2550–3.
[24] Yang S, Man HC, Xing W, Zheng X. Adhesion strength of plasma-sprayed hydroxyapatite coatings on laser gas-nitrided pure titanium. Surf Coat Tech 2009;203:3116–22.
[25] Moulder JF, Stickle WF, Sobol PE, Bomben KD. Handbook of X-ray photoelectron spectroscopy. Eden Prairie, MN, USA: Perkin-Elmer Corporation, Physical Electronics Division; 1992.
[26] Massalski TB. Binary alloy phase diagrams. 2nd ed. Materials Park, Ohio, USA: ASM International; 1990.
[27] Kutsenko L, Fuks D, Kiv A, Burlaka L, Talianker M, Monteiro O, et al. Structural changes in Mg alloy induced by plasma immersion ion implantation of Ag. Acta Mater 2004;52:4329–35.
[28] Monteiro OR. Thin film synthesis by energetic condensation. Annu Rev Mater Res 2001;31:111–37.
[29] Kutsenko L, Fuks D, Kiv A, Burlaka L, Talianker M, Monteiro O, et al. Mechanism of phase transformations in Mg-based alloys subjected to plasma immersion ion implantation of Ag. Acta Mater 2006;54:2637–43.
[30] Cai K, Frant M, Bossert J, Hildebrand G, Liefeith K, Jandt KD. Surface functionalized titanium thin films: zeta-potential, protein adsorption and cell proliferation. Colloid Surf B 2006;50:1–8.
[31] Lok CN, Ho CM, Chen R, He QY, Yu WY, Sun H, et al. Silver nanoparticles: partial oxidation and antibacterial activities. J Biol Inorg Chem 2007;12:527–34.
[32] Su HL, Chou CC, Hung DJ, Lin SH, Pao IC, Lin JH, et al. The disruption of bacterial membrane integrity through ROS generation induced by nanohybrids of silver and clay. Biomaterials 2009;30:5979–87.
[33] AshaRani PV, Hande MP, Valiyaveettil S. Anti-proliferative activity of silver nanoparticles. BMC Cell Biol 2009;10:65.
[34] Anselme K. Osteoblast adhesion on biomaterials. Biomaterials 2000;21:667–81.
[35] Lee YJ, Park SJ, Lee WK, Ko JS, Kim HM. MG63 osteoblastic cell adhesion to the hydrophobic surface precoated with recombinant osteopontin fragments. Biomaterials 2003;24:1059–66.
[36] Rai M, Yadav A, Gade A. Silver nanoparticles as a new generation of antimicrobials. Biotechnol Adv 2009;27:76–83.
[37] Hussain SM, Hess KL, Gearhart JM, Geiss KT, Schlager JJ. In vitro toxicity of nanoparticles in BRL 3 a rat liver cells. Toxicol in Vitro 2005;19:975–83.
[38] Navarro E, Piccapietra F, Wagner B, Marconi F, Kaegi R, Odzak N, et al. Toxicity of silver nanoparticles to chlamydomonas reinhardtii. Environ Sci Technol 2008;42:8959–64.
[39] Vanýsek P. Electrochemical series. CRC Press LLC; 2000.
[40] Liu LJ, Schlesinger M. Corrosion of magnesium and its alloys. Corros Sci 2009;51:1733–7.
[41] Song G, Johannesson B, Hapugoda S, StJohn D. Galvanic corrosion of magnesium alloy AZ91D in contact with an aluminium alloy, steel and zinc. Corros Sci 2004;46:955–77.
[42] Carraro C, Maboudian R, Magagnin L. Metallization and nanostructuring of semiconductor surfaces by galvanic displacement processes. Surf Sci Rep 2007;62:499–525.
[43] Qian S, Zhang J, Qu D. Theoretical and experimental study of microcell and macrocell corrosion in patch repairs of concrete structures. Cement Concrete Comp 2006;28:685–95.
[44] Arslan H, Celikkan H, OrnekN Ozan O, Ersoy AE, Aksu ML. Galvanic corrosion of titanium-based dental implant materials. J Appl Electrochem 2008;38:853–9.
[45] Warkus J, Raupach M, Gulikers J. Numerical modelling of corrosion-theoretical backgrounds. Mater Corros 2006;57:614–7.
[46] Guseva O, Schmutz P, Suter T, Trzebiatowski O. Modelling of anodic dissolution of pure aluminium in sodium chloride. Electrochim Acta 2009;54:4514–24.
[47] Shannon RD. Revised effective ionic radii and systematic studies of interatomic distances in halides and chalcogenides. Acta Crystallogr A 1976;32:751–67.
[48] Vu B, Chen M, Crawford RJ, Ivanova EP. Bacterial extracellular polysaccharides involved in biofilm formation. Molecules 2009;14:2535–54.
[49] Boyer PD. The ATP synthase-a splendid molecular machine. Annu Rev Biochem 1997;66:717–49.
[50] Ballmoos C. Alternative proton binding mode in ATP synthases. J Bioenerg Biomembr 2007;39:441–5.
[51] Trumpower BL, Gennis RB. Energy transduction by cytochrome complexes in mitochondrial and bacterial respiration: the enzymology of coupling electron transfer reactions to transmembrane proton translocation. Annu Rev Biochem 1994;63:675–716.
[52] Lok C, Ho C, Chen R, He Q, Yu W, Sun H, et al. Proteomic analysis of the mode of antibacterial action of silver nanoparticles. J Proteome Res 2006;5:916–24.
[53] Schultz BE, Chan SI. Structures and proton-pumping strategies of mitochondrial respiratory enzymes. Annu Rev Biophys 2001;30:23–65.
[54] Vellai T, Vida G. The origin of eukaryotes: the difference between prokaryotic and eukaryotic cells. Proc R Soc Lond B 1999;266:1571–7.